Effect of grain orientation and grain size on ferroelectric domain switching and evolution: Phase field simulations

S. Choudhury [a,*], Y.L. Li [a,b], C. Krill III [c], L.Q. Chen [a]

[a] Department of Materials Science and Engineering, Penn State University, University Park, PA 16802, United States
[b] MPA-STC, MS K763, Los Alamos National Lab, Los Alamos, NM 87545, United States
[c] Materials Division, University of Ulm, Albert-Einstein-Allee 47, D89081 Ulm, Germany

Abstract

Phase field simulations were conducted in order to understand the effect of grain orientation, grain boundary and grain size on ferroelectric domain switching, stress distribution and evolution behavior under an applied electric field. Tetragonal ferroelectric domains were considered. Hysteresis loops were obtained for a single crystal, a bi-crystal and a polycrystal and the differences in their coercive fields were examined. It was found that the magnitude of the coercive field was closely related to the domain structures at the maximum electric field. Nucleation of new domains at a grain boundary led to local high stress. The effect of a reduced ferroelectric transition temperature at the grain boundary on the polarization distribution, domain structure and switching was studied.
© 2006 Acta Materialia Inc. Published by Elsevier Ltd. All rights reserved.

Keywords: Ceramics; Phase field models; Grain boundaries; Ferroelectricity

1. Introduction

Ferroelectric ceramics are used in microelectronics where the switching behavior of ferroelectrics under an applied electric field is exploited [1]. It has been observed that the domain structure and domain wall mobility play a significant role in determining the switching behavior in these materials [2]. Furthermore, the dielectric permittivity, coercive field and remnant polarization [2–6] have been found to be strongly dependent on the grain size of ceramics. The change in properties with grain size was primarily attributed to the mechanical stresses developed at the grain boundary [7]. In this context, it is important to understand the role of the grain boundary in determining the domain structure and switching behavior in ferroelectric ceramics.

However, it is often difficult to separate the role of grain boundaries in determining the domain structure and ferroelectric properties from other factors experimentally, for example, the space charge, grain boundary phases and porosity arising from different processing conditions [2,8,9]. In particular, it has been observed that the presence of a low permittivity non-ferroelectric grain boundary layer decreases the dielectric properties in barium titanate ceramics [9]. Besides the grain boundary and grain boundary phases, grain orientation has been found to play a significant role in polarization switching [10]. The preferential orientation of grains has been shown to affect the properties in ferroelectric ceramics [11]. Thus, the objective of this paper was to examine the roles of the grain orientation, grain boundary and presence of a low ferroelectric transition temperature at the grain boundary on the domain structure, stress distribution and switching behavior in ferroelectric materials during polarization switching.

There have been a number of computer simulations of domain evolution during ferroelectric transition as well as

---

* Corresponding author. Tel.: +1 814 865 0389.
  E-mail address: sxc398@psu.edu (S. Choudhury).

domain evolution during an applied field in both single crystal bulk and thin film systems [10,12–15]. There have also been several theoretical studies of the switching behavior of ferroelectric polycrystals [16–18]. These models typically assumed that ferroelectric polycrystals are made up of an array of single domain grains and the ferroelectric or ferroelastic switching occurs when the energy provided by the applied field exceeds a critical value. Kim [19] proposed a continuum model for investigating the effects of grain boundaries on the switching behavior using a one-dimensional model. Rodel and Kreher [20] presented a micro-mechanical model for showing the effect of the orientations of crystallites in ferroelectric ceramics on switching assuming a laminar domain structure. Recently Zhang and Bhattacharya [10,21] presented a phase field model for domain switching in single- and bi-crystals. It was shown that the domain switching behavior was dependent on the misorientation of the two half crystals in the bi-crystal. Li et al. [22] showed that the domain switching in a grain was constrained by the neighboring grains. The authors recently proposed a phase field model for predicting the polarization switching and domain structure evolution under an applied electric field in ferroelectric polycrystals [23]. In particular, the role of grain boundaries in the nucleation and growth of new domains was studied. It was shown that switching took place through the nucleation of 90° domains at grain boundaries and subsequent growth into the grain interiors instead of direct 180° domain switching. A correlation between the domain structures in neighboring grains was observed and polarization switching in one grain was found to affect the switching in neighboring grains.

In this paper, we conducted extensive phase field simulations for studying the effect of the grain orientation, grain boundary and a low ferroelectric transition temperature at the grain boundary on the domain structure, stress distribution and switching behavior in ferroelectric materials. Hysteresis loops were constructed for a single crystal, a bi-crystal and a polycrystal. Coercive fields obtained from phase field simulations were compared with thermodynamic calculations assuming single-domain and experimentally observed coercive fields. We employed $PbTiO_3$ as a model system. The paper is organized as follows: Section 2 gives a brief description of the phase field model, the methodology of the analytical calculations and the choice of the parameters for simulation are given in Section 3 and the numerical results and discussions are presented in Section 4.

2. Phase field model of ferroelectric domain structures in polycrystals

There are two levels of structure for describing the microstructure in ferroelectric ceramics, i.e. the grain structure and the domain structure of each individual grain. A description of the grain structure is presented in Section 4.3. The domain structure is described by the inhomogeneous distribution of local polarization P_i^L, where P_1^L, P_2^L and P_3^L are the components of the polarization vector in the local crystallographic coordinate system within a grain and the superscript L denotes the local coordinates (see Fig. 1(a)). The total free energy of a ferroelectric polycrystal is given by

$$F = \int_V (f_{bulk} + f_{elas} + f_{grad} + f_{elec}) \, dV, \tag{1}$$

where f_{bulk} is the local bulk free energy density, f_{elas} is the elastic energy density, f_{grad} is the gradient energy density which is only non-zero around domain walls and grain boundaries and f_{elec} is the electrostatic energy density. V is the volume of the polycrystal considered.

The bulk free energy density in a given grain is expanded in terms of polarization components using the Landau theory, i.e.
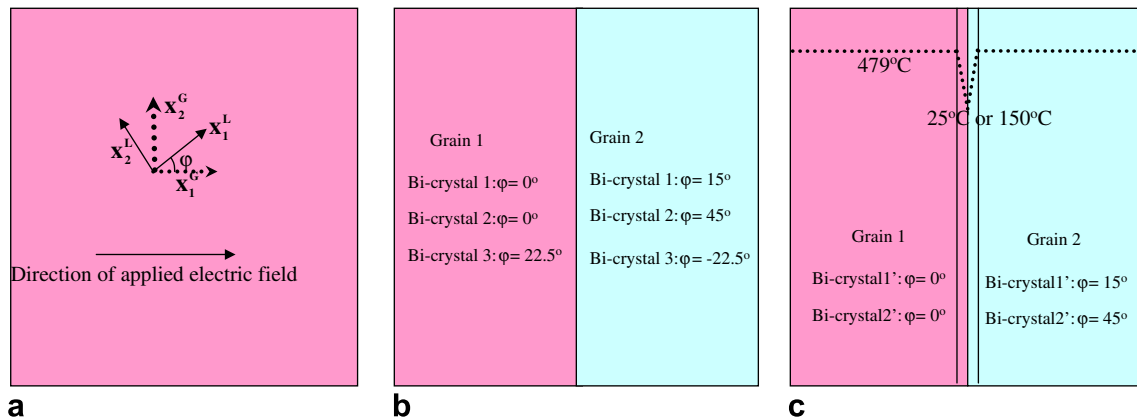

Fig. 1. (a) Schematic diagram of single crystal with the two different coordinate systems. G and L represent the global and local coordinates, respectively. The global coordinate system is fixed. The orientation angle φ varies between 0° and 45°. (b) Schematic diagram of a bi-crystal. The considered orientations of grain 1 and 2 are listed. (c) Schematic diagram of a bi-crystal with reduced transition temperature at the grain boundary. The transition temperature is varied linearly between the grain boundary and grain. The lowest transition temperature at the grain boundary is maintained either at 25 °C or 150 °C for $PbTiO_3$. The grain boundary width is same for all bi-crystals with reduced transition temperature at the grain boundary.

$$f_{\text{bulk}} = \alpha_1[(P_1^L)^2 + (P_2^L)^2 + (P_3^L)^2] + \alpha_{11}[(P_1^L)^4 + (P_2^L)^4 + (P_3^L)^4]$$
$$+ \alpha_{12}[(P_1^L P_2^L)^2 + (P_2^L P_3^L)^2 + (P_3^L P_1^L)^2]$$
$$+ \alpha_{111}[(P_1^L)^6 + (P_2^L)^6 + (P_3^L)^6]$$
$$+ \alpha_{112}[(P_1^L)^2\{(P_2^L)^4 + (P_3^L)^4\} + (P_2^L)^2\{(P_3^L)^4 + (P_1^L)^4\}$$
$$+ (P_3^L)^2\{(P_1^L)^4 + (P_2^L)^4\}] + \alpha_{123}(P_1^L P_2^L P_3^L)^2 \quad (2)$$

where α_1, α_{11}, α_{12}, α_{111}, α_{112}, and α_{123} are the dielectric and higher order stiffnesses of the single crystal under a stress-free boundary condition. They can be found in Ref. [24] for lead titanate.

By definition, a ferroelectric material develops a spontaneous polarization during its transformation from its paraelectric state to a ferroelectric state when it is cooled below the Curie temperature. This transformation leads to a spontaneous strain that is related to the spontaneous polarization through the electro-strictive coefficient Q_{ijkl},

$$\varepsilon_{ij}^{0L} = Q_{ijkl}P_k^L P_l^L, \quad (3)$$

where the repeated subscripts imply Einstein summation and this convention is used for the whole paper except indicated exceptions. For a polycrystalline system it is necessary to describe the spontaneous strains in different grains using a common reference coordinate system, which we call the global coordinate system. The two coordinate systems, namely the global and the local coordinate systems, are shown in Fig. 1(a) for a two-dimensional single crystal. A transformation matrix $\text{TR} = (tr_{ij})$ determining the relationship between the tensor components of property in the global coordinate system denoted by a superscript G and those in the local coordinate system within each grain was given in Ref. [23]. For example, for a grain rotated by an angle φ about the x_3^G axis only the transformation matrix is given by

$$\text{TR} = \begin{pmatrix} \cos[\varphi] & \sin[\varphi] & 0 \\ -\sin[\varphi] & \cos[\varphi] & 0 \\ 0 & 0 & 1 \end{pmatrix}. \quad (4)$$

Being a second-rank tensor, the spontaneous strain in the global system is related to that in the local system by

$$\varepsilon_{ij}^{0G} = tr_{ki}tr_{lj}\varepsilon_{kl}^{0L}. \quad (5)$$

The elastic energy density is given by

$$f_{\text{elas}} = \frac{1}{2}C_{ijkl}e_{ij}^G e_{kl}^G = \frac{1}{2}C_{ijkl}(\varepsilon_{ij}^G - \varepsilon_{ij}^{0G})(\varepsilon_{kl}^G - \varepsilon_{kl}^{0G}), \quad (6)$$

where $e_{ij}^G = (\varepsilon_{ij}^G - \varepsilon_{ij}^{0G})$ is the elastic strain, ε_{ij}^G is the total strain compared to the parent paraelectric phase and C_{ijkl} is the elastic stiffness tensor.

The total strain field ε_{ij}^G can be written as the sum of the spatially independent homogenous strain $\bar{\varepsilon}_{ij}^G$ and a spatially dependent heterogeneous strain field $\delta\varepsilon_{ij}^G$, i.e.

$$\varepsilon_{ij}^G = \bar{\varepsilon}_{ij}^G + \delta\varepsilon_{ij}^G. \quad (7)$$

The homogenous strain determines the macroscopic shape deformation of the entire polycrystal due to an applied strain, phase transformations or domain structure changes. In this work, the external boundary of the polycrystal was either clamped or stress free. For the clamped boundary condition the homogenous strain ($\bar{\varepsilon}_{ij}^G$) is zero. By assuming that elastic constants are independent of space, the homogenous strain under the stress-free boundary condition is obtained as the spatial average of eigen strain, i.e. $\bar{\varepsilon}_{kl}^G = \bar{\varepsilon}_{kl}^{0G}$, where $\bar{\varepsilon}_{kl}^{0G} = \frac{1}{V}\int_V \varepsilon_{kl}^{0G} dV$. The heterogeneous strain is defined in such a way that $\int_V \delta\varepsilon_{ij}^G dV = 0$. The heterogeneous strain is spatially dependent and is obtained by solving the mechanical equilibrium equation $\sigma_{ij,j}^G = 0$ using periodic boundary conditions, where σ_{ij}^G denotes the elastic stress component and $\sigma_{ij}^G = C_{ijkl}(\varepsilon_{kl}^G - \varepsilon_{kl}^{0G})$. A detailed method of solving the inhomogeneous strain was described in a previous paper [23].

The contribution of the domain walls to the total free energy, i.e. the domain wall energy, is introduced through the gradient of the global polarization field. For simplicity we assumed the gradient energy to be isotropic. Hence, the gradient energy density can be written as

$$f_{\text{grad}} = \frac{1}{2}G_{11}((P_{1,1}^G)^2 + (P_{1,2}^G)^2 + (P_{1,3}^G)^2 + (P_{2,1}^G)^2$$
$$+ (P_{2,2}^G)^2 + (P_{2,3}^G)^2 + (P_{3,1}^G)^2 + (P_{3,2}^G)^2 + (P_{3,3}^G)^2), \quad (8)$$

where G_{11} is the gradient energy coefficient and $P_{i,j}^G$ represents spatial differentiation of polarization, i.e. $P_{i,j}^G = \partial P_i^G/\partial x_j^G$.

Under an applied electric field the electrostatic energy density f_{elec} consists of three contributions, i.e. the dipole–dipole interaction energy density f_{dipole}, the depolarization energy density f_{depol} and the energy density due to the applied electric field f_{appel}, i.e.

$$f_{\text{elec}} = f_{\text{dipole}} + f_{\text{depol}} + f_{\text{appel}}. \quad (9)$$

For an electrically inhomogeneous system the long-range electric dipole–dipole interaction energy density is given by

$$f_{\text{dipole}} = -\frac{1}{2}E_i^G P_i^G, \quad (10)$$

where E_i^G is the inhomogeneous electric field due to dipole–dipole interactions in the global coordinates. It is related to the electric displacement D_i^G through the usual relation $D_i^G = \varepsilon_0\kappa_{ij}E_j^G + P_i^G$, in which $\varepsilon_0 = 8.85 \times 10^{-12}$ Fm^{-1} is known as the dielectric permittivity of the vacuum and κ_{ij} is the relative dielectric permittivity. Assuming there is no space charge, the electric displacement D_i^G satisfies the electrostatic equilibrium equation of $D_{i,i}^G = 0$. For a given polarization distribution the electric field components E_i^G and the electric displacements D_i^G are solved by using Fourier transforms. A detailed method of solving the inhomogeneous electric field was described in a previous paper [23].

The average depolarization field in the global coordinate due to the presence of surface charges can be approximated as

$$E_{i,\text{depol}}^{\text{G}} = -\frac{1}{\varepsilon_i}\overline{P_i^{\text{G}}}, \tag{11}$$

where $\overline{P_i^{\text{G}}}$ is the spatial average of the i-th component of polarization in the global coordinates and $\varepsilon_i = \varepsilon_0 \kappa_{ij}$ where the repeated index, as well as in Eq. (11), does not imply summation. Hence the depolarization energy density is given by

$$f_{\text{depol}} = -\frac{1}{2}E_{i,\text{depol}}^{\text{G}}P_i^{\text{G}}. \tag{12}$$

When an externally electric field $E_{\text{appel}}^{\text{G}}$ is applied an additional contribution f_{appel} should be taken into consideration:

$$f_{\text{appel}} = -E_{i,\text{appel}}^{\text{G}}P_i^{\text{G}}. \tag{13}$$

With the total free energy as a function of the global polarization, the temporal evolution of polarization as well as the domain structure is obtained by solving the time-dependent Ginzburg–Landau (TDGL) equation:

$$\frac{\partial P_i^{\text{G}}(\mathbf{x}^{\text{G}}, t)}{\partial t} = -M\frac{\delta F}{\delta P_i^{\text{G}}(\mathbf{x}^{\text{G}}, t)}, \quad i = 1, 2, 3, \tag{14}$$

where M is a kinetic coefficient related to the domain mobility and t is the time.

3. Analytical calculations and numerical simulations

Assuming a single tetragonal domain for the ferroelectric state, the hysteresis loops under clamped boundary conditions can be computed analytically for a single crystal at different orientations. The dipole–dipole interaction energy, depolarization energy and the gradient energy vanish for a single domain system. Thus, under a clamped boundary condition and assuming a single domain state, the total energy of the system can be defined as the sum of the bulk, the elastic energy and electric energy due to the applied electric field. The hysteresis loop is computed analytically by minimizing the total energy with respect to P_1^{G}. Thus, the applied electric field along the x_1^{G} direction is expressed as a function of P_1^{G} and is calculated as $E_{1,\text{appel}}^{\text{G}} = \partial F^0/\partial P_1^{\text{G}}$, where F^0 is the sum of the bulk and the elastic energies.

The temporal evolution of the global polarization vector fields is obtained by solving Eq. (14) numerically with the semi-implicit Fourier spectral method [25]. The local polarization components are obtained from the global polarization components using the relation $P_i^{\text{L}} = \text{tr}_{ij}P_j^{\text{G}}$. In the computer simulation we employed 128×128 discrete grid points and periodic boundary conditions were applied along the x_1^{G} and x_2^{G} axes. The grid space was chosen to be $\Delta x_1^{\text{G}} = \Delta x_2^{\text{G}} = l_0$, where $l_0 = \sqrt{G_{110}/\alpha_0}$, $G_{110} = 1.73 \times 10^{-10}$ C^{-2} m^4 N and $\alpha_0 = |\alpha_1|_{T=25\,°C}$. Hence, the grid spacing in real space was about $\Delta x_1^{\text{G}} = \Delta x_2^{\text{G}} = 1$ nm. The methodology of calculating the real grid spacing was described in a previous paper [15]. We took the gradient energy coefficient to be $G_{11}/G_{110} = 0.6$. The time step for the evolution in Eq. (14) is $\Delta t/t_0 = 0.05$, where $t_0 = 1/(\alpha_0 M)$. For the elas-

tic energy calculation we assumed the elastic stiffness tensor to be isotropic with shear modulus $\mu = 0.476 \times 10^{11}$ N m^{-2} and Poisson's ratio $v = 0.312$, while for the dipole–dipole interaction energy calculation we used $\kappa_{11} = \kappa_{22} = 100$ in our simulations. It should be pointed out that, although we assumed uniform dielectric constants, there was a spatial dependence of the apparent dielectric constant due to the spatial dependence of the spontaneous polarization. However, a more accurate calculation should use a spatially varying dielectric constant tensor with the dielectric constant locally evaluated from the inverse of the second derivative of free energy with respect to polarization. Spatially varying the dielectric constant would significantly complicate the solution of the electrostatic equilibrium equation since the dielectric constant tensor would have a tetragonal symmetry with tetragonal axes along different directions in different domains.

A domain structure was first generated by performing the simulations without any applied electric field, starting from an initial paraelectric state with small random perturbations. The depolarizing field was considered along both x_1^{G} and x_2^{G} directions. In order to construct the PE loop an electric field was then applied to the generated domain structure in the x_1^{G} direction while a depolarizing field was considered only along the x_2^{G} direction as we assumed that the electrodes fully compensated the bound charges in the x_1^{G} direction. The domain structure from a previous simulation was used as the input at each increment of the electric field. The PE loop was obtained by plotting the normalized average polarization ($\overline{P_1^{\text{G}}}/P_0$) versus the normalized electric field in the x_1^{G} direction (E_1^{G}/E_0), where $E_0 = \alpha_0 P_0 = 1.306 \times 10^8$ V cm^{-1} and $P_0 = |P|_{T=25\,°C} = 0.757$ C m^{-2}.

4. Results and discussions

4.1. Ferroelectric domain switching in single crystals

We analytically calculated the hysteresis loops of a single crystal under clamped boundary conditions for two different orientations (0° and 45°) with respect to the applied electric field and the broken lines in Fig. 2 show the corresponding loops. As expected, the coercive field along the 45° orientation was $\sqrt{2}$ times larger than the 0° orientation. However, as it is well known that multi-domains form during a ferroelectric phase transition, it can be expected that the switching of a single crystal with multi-domains is very different from that of a single-domain crystal. The solid lines in Fig. 2 show the hysteresis loops for single crystals under the clamped boundary condition at different orientations obtained from simulations as an electric field was applied along the x_1^{G} direction. Each point in the PE loop represents the average polarization at the end of 10,000 iterations at a given electric field. It is shown that, as the angle φ increased, the coercive field increased.

It is interesting to observe that there was a significant jump in the coercive field between $\varphi = 20°$ and 30°. The
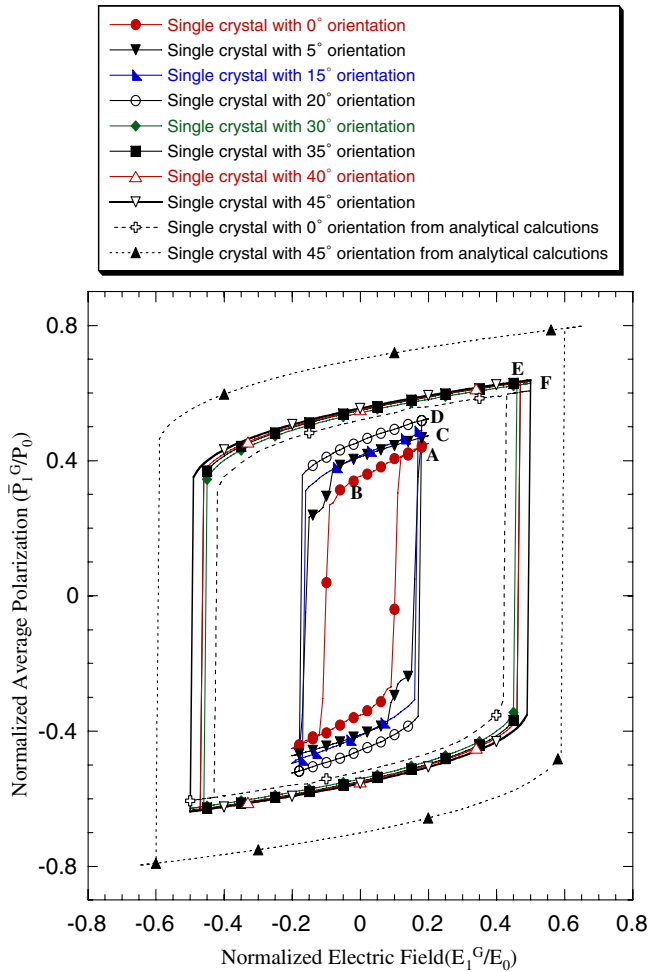
Fig. 2. Hysteresis loops of single crystals with different orientations obtained from the phase-field simulations and the analytical calculations. The solid and the dotted lines indicate the hysteresis loops obtained from phase-field simulations and analytical calculations, respectively. Angles in the legend denote the orientations of the single crystals with the applied electric field.

reason for such a jump can be found by examining the domain structures in Fig. 3. There are four tetragonal variants in a typical tetragonal domain structure simulated in two dimensions. We labeled the four variants as a_1 positive, a_2 positive, a_1 negative and a_2 negative with polarizations $(P_1^L > 0, P_2^L = P_3^L = 0)$, $(P_2^L > 0, P_1^L = P_3^L = 0)$, $(P_1^L < 0, P_2^L = P_3^L = 0)$ and $(P_2^L < 0, P_1^L = P_3^L = 0)$, respectively. The four variants are represented with the different shades shown in Fig. 3. The arrows represent the directions of the polarization vectors. Fig. 3(a) represents the domain structure for $\varphi = 0°$ at the maximum electric field corresponding to position A in Fig. 2. As can be seen, the domain structure consists of three types of domains: a_1 positive, a_2 positive and a_2 negative. Fig. 3(b) shows the domain structure for $\varphi = 0°$ that corresponds to point B in Fig. 2. It shows the nucleation of new domains at the twin boundary through 90° domain switching (marked by the circles). Similarly, the domain structures for $\varphi = 15°$ and 20° at the maximum applied electric fields (points C and D in

Fig. 2) also display three types of domain (Fig. 3(c) and (d)). By comparing Fig. 3(a), (c) and (d) we found that $\varphi = 20°$ has a smaller volume fraction of the a_2-positive domain. On the other hand, when φ was greater than 30° there were only two types of domains at the maximum applied electric field, namely a_1 positive and a_2 negative (Fig. 3(e) and (f)). The absence of the third type of domain was the main reason for the significant increase in the coercive field for φ greater than 30° (Fig. 2).

In order to study the effect of the external mechanical boundary conditions on the switching behavior, we considered two single crystals with different orientations under stress-free boundary conditions and the PE loops are shown in Fig. 4. The dotted and solid lines show the hysteresis loops obtained from thermodynamic calculations and phase field simulations, respectively. For comparison, hysteresis loops of single crystals obtained from thermodynamic calculation under clamped boundary condition are also presented. The figure shows that, similar to the clamped boundary condition, the coercive field obtained from the thermodynamic calculation increased as the angle φ increased. Contrary to the thermodynamic calculation the coercive field obtained from the phase field simulation under a stress-free condition decreased as the angle φ increased. This can be explained from the domain structure corresponding to the maximum electric field as shown in Fig. 5. The figure shows that, for $\varphi = 0°$, the single crystal was comprised of a single domain, while for $\varphi = 45°$ the domain structure was comprised of two kinds of domain, which facilitated the formation of new domains during polarization switching. This observed decrease in the coercive field with the presence of more than one tetragonal variant in a single crystal was similar to the trend observed under a clamped boundary condition as presented above. Comparison of the domain structures obtained under the stress-free and clamped boundary conditions showed that it was easier to stabilize more than one tetragonal variant under the clamped boundary condition. Since neighboring grains in a polycrystal clamp a crystalline grain, we will assume a clamped boundary condition for the rest of the paper.

4.2. Switching in bi-crystals

Fig. 1(b) shows a schematic diagram of two bi-crystals. In both bi-crystals, the orientation (φ) of grain 1 is 0° while that of grain 2 is 15° for bi-crystal 1 and 45° for bi-crystal 2.

Fig. 6(a) and (b) shows the hysteresis loops for bi-crystal 1 and bi-crystal 2, respectively. For comparison, we have also included the hysteresis loops for the corresponding single crystals at different orientations. It is shown that the hysteresis loop for bi-crystal 1 lies in between those for the corresponding single crystal values with the coercive field approximately the average of the single crystal values, i.e. the effect of the grain boundary is minimal. However, for bi-crystal 2 the coercive field was much lower than the average of the corresponding single crystals as shown in Fig. 6(b).
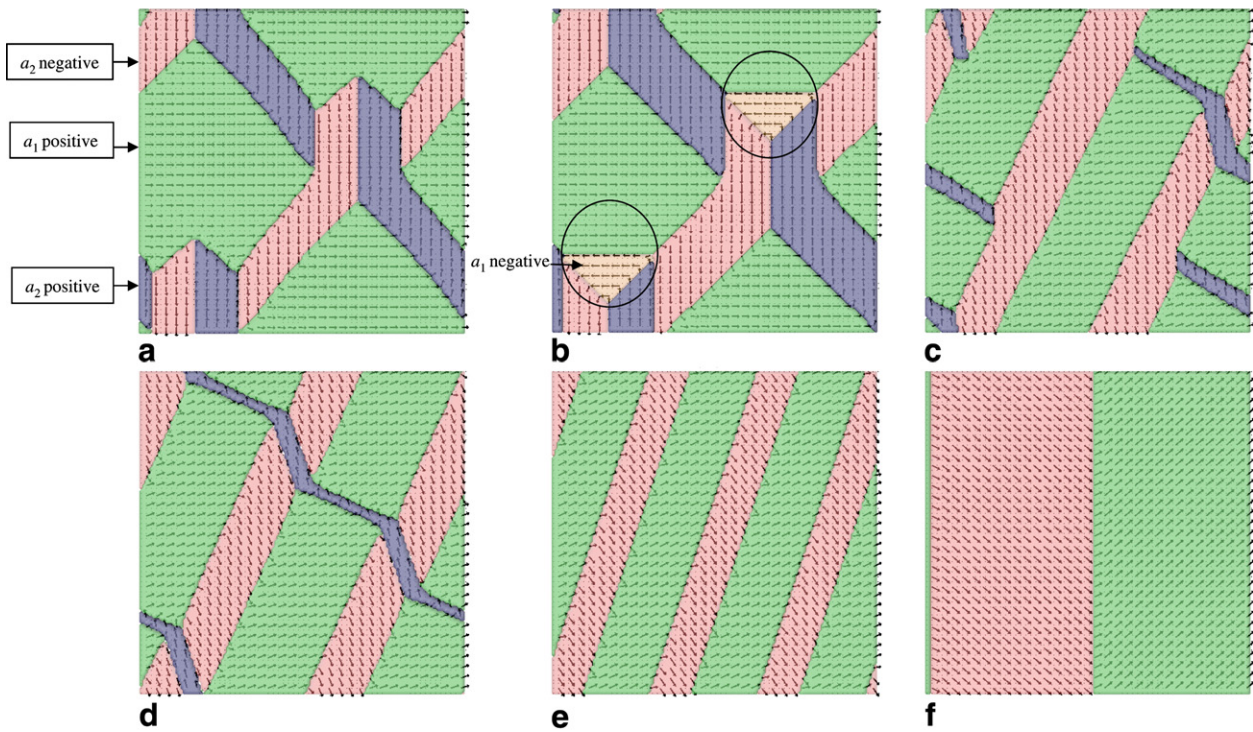
Fig. 3. Domain structures of the single crystals with different orientations presented in Fig. 2 for various stages of polarization switching: (a) for $\varphi = 0°$ at point A; (b) for $\varphi = 0°$ at point B; (c) for $\varphi = 15°$ at point C; (d) for $\varphi = 20°$ at point D; (e) for $\varphi = 30°$ at point E; (f) for $\varphi = 45°$ at point F.

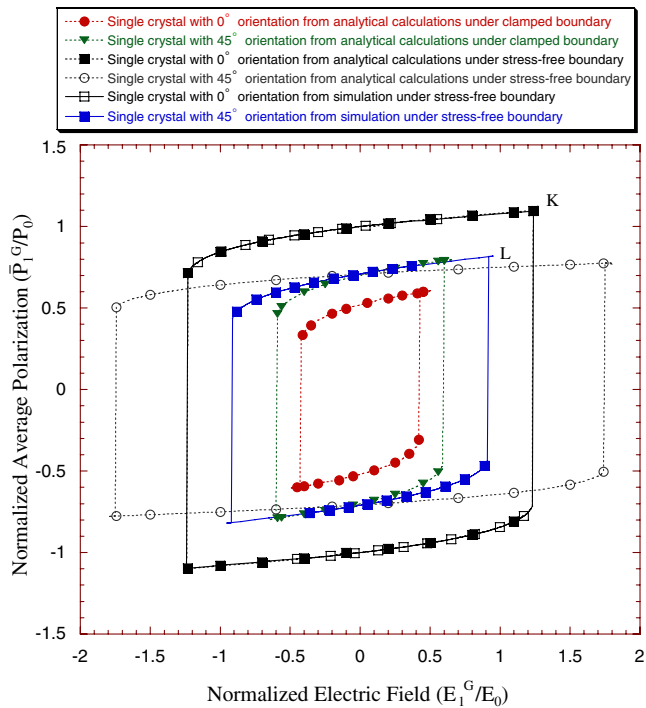Fig. 4. Hysteresis loops of the single crystals with different orientations under the stress-free condition.

In order to understand the difference between the switching behaviors of the two bi-crystals, we examined the domain structure (Fig. 7(a)) of bi-crystal 1 at the max-

imum applied electric field (point M in Fig. 6(a)). It is shown that each grain consisted of three domains, similar to their corresponding single crystals at the same orientations. Fig. 7(b) is a domain structure during initiation of switching in the bi-crystal corresponding to point N in Fig. 6(a). A new domain is shown to nucleate at the grain boundary. For comparison, we present the domain structure of bi-crystal 2 at the maximum applied electric field in Fig. 7(c) (point X in Fig. 6(b)). It is seen that, although the domain structure in grain 1 has three types of domain, grain 2 with $\varphi = 45°$ contains only two types of domain. However, in this case nucleation of a new domain occurs during switching at the grain boundary (Fig. 7(d)), which corresponds to point Y in Fig. 6(b) and it propagates towards the grain interior. Hence, although grain 2 in bi-crystal 2 consisted of only two domains at the maximum applied field, the presence of the grain boundary acted as a source for nucleating new domains. As a result, the coercive field was much lower than the average of the corresponding single crystals (Fig. 6(b)).

In the above two examples, both of them had one of the two half crystals oriented along φ equal to 0. As another example, we examined the switching behavior of a bi-crystal with 45° misorientation between the two half crystals. One half crystal is oriented at $\varphi = 22.5°$ and the other half is oriented at $\varphi = -22.5°$. We call this example bi-crystal 3. Fig. 7(e) shows the domain structure at the maximum applied electric field (point Z in Fig. 6(c)). It is shown that both grains contained three types of domain. Thus, when
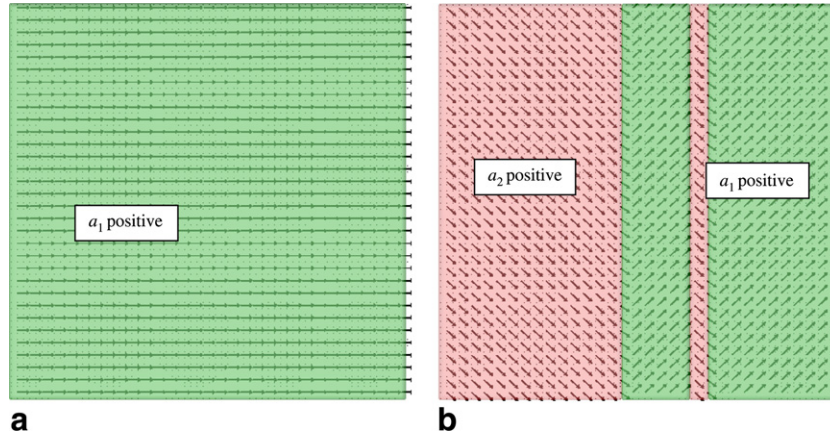
Fig. 5. Domain structures of the single crystals obtained from simulations under the stress-free condition corresponding to the maximum electric field: (a) for single crystal with $\varphi = 0°$ at point K; (b) for single crystal with $\varphi = 45°$ at point L in Fig. 4.
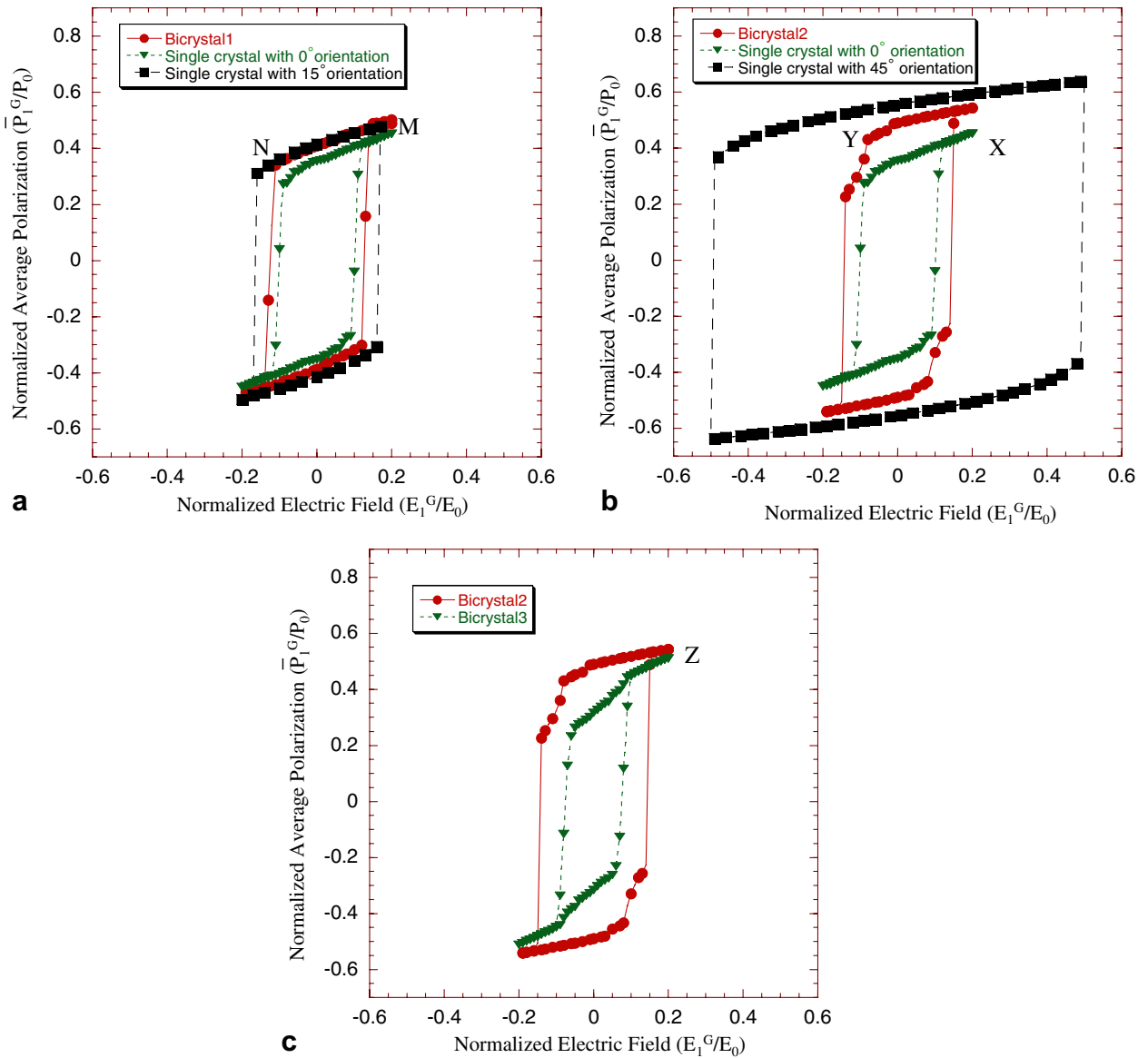

Fig. 6. Hystersis loops of the bi-crystals shown in Fig. 1(b). The hystersis loops of the single crystals obtained from simulation for $\varphi = 0°$ and 15°, $\varphi = 0°$ and 45° are presented in (a) and (b), respectively, for comparison. Plots in (c) show, for comparison, the hystersis loops of bi-crystal 2 and bi-crystal 3.
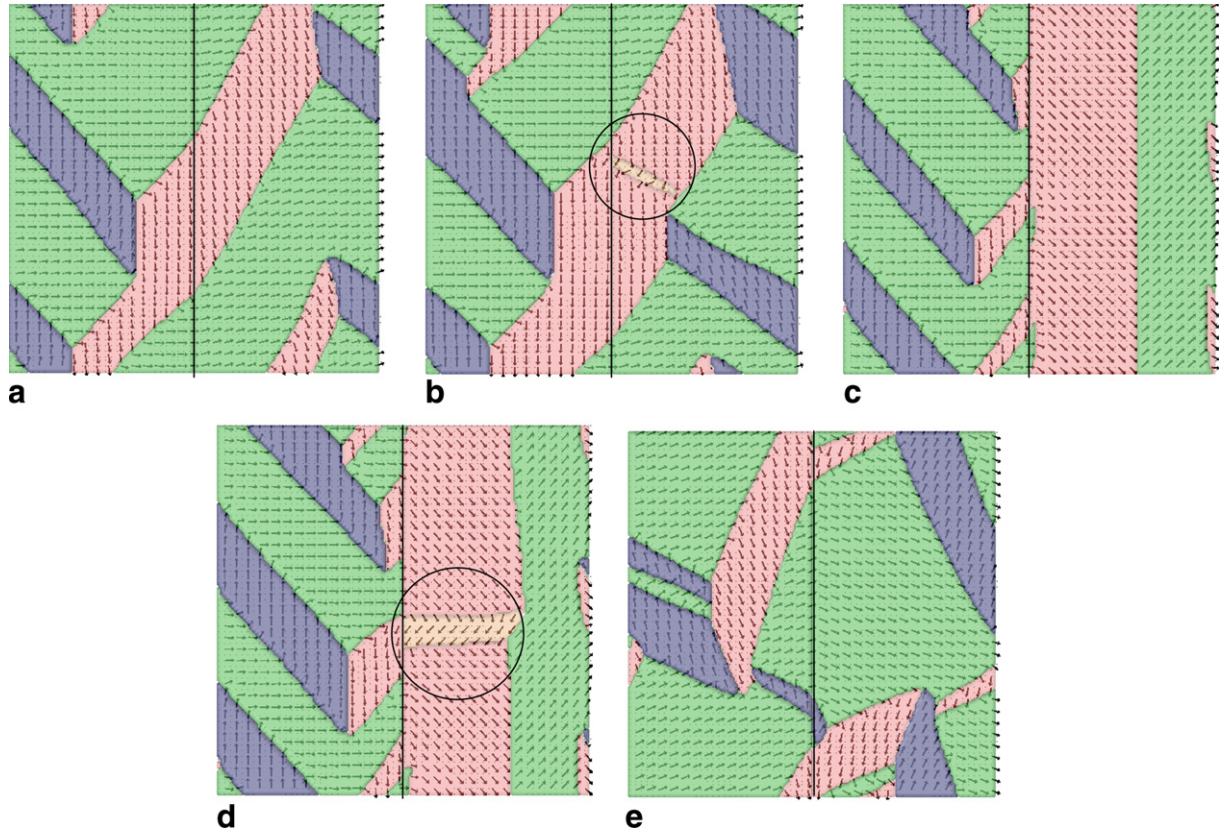
Fig. 7. Domain structures of bi-crystals at various stages of polarization switching presented in Fig. 6. Domain structures in (a) and (b) are, respectively, corresponding to point M and point N of bi-crystal 1 in Fig. 6(a). Domain structures in (c) and (d) are, respectively, corresponding to point X and point Y of bi-crystal 2 in Fig. 6(b). The circles represent the nucleated new domains near the grain boundaries. The domain structure in (e) corresponds to points Z of bi-crystal 3 in Fig. 6(c).

the electric field was reversed, new domains could nucleate at twin boundaries and, consequently, the coercive field in bi-crystal 3 was less than the coercive field for bi-crystal 2 (Fig. 6(c)). Furthermore, a comparison between the slopes of the hysteresis loops from the two bi-crystals showed that nucleation of the new domain during switching initiated at a much lower field at a twin boundary in bi-crystal 3 than at the grain boundary as in bi-crystal 2.

In order to study the effect of grain boundaries on the stress distribution during polarization switching, we plotted the distribution of normalized global elastic stress near the grain boundary in bi-crystal 1 and bi-crystal 2. The corresponding stress distributions are shown in Fig. 8. The elastic stress components σ_{ij}^{G} were calculated from the elastic strains using the relation $\sigma_{ij}^{G} = C_{ijkl}e_{kl}^{G}, i,j,k,l = 1,2,3$. Fig. 8(a)–(c) displays the distribution of the stress components in bi-crystal 1 corresponding to the domain structure presented in Fig. 7(b). Solid lines mark the grain boundary while the domain walls are schematically shown by dotted lines. The high-stress location near the grain boundary is marked. The fact that high stresses occurred near the grain boundary could be related to the nucleation of the new domain. The distributions of the stress components in bi-crystal 2 (based on the domain structure presented in Fig. 7(d)) are shown in Fig. 8(d)–(f). Similar to bi-crystal

1, high stress was generated near the grain boundary during polarization switching. Comparing the stress distribution for the two bi-crystals, the magnitude of the stress components was higher in bi-crystal 2 with a larger misalignment between the two grains. Nucleation of the new domain at a grain boundary created intersections between the domain boundaries and a grain boundary. The domains around the intersections had different transformation strains as a result of different crystallographic orientations. The incompatibility of the deformation among these domains near the grain boundary resulted in a high stress concentration at the intersections.

4.2.1. Effect of a reduced transition temperature at grain boundaries

In order to study the effect of the non-ferroelectric phase of a grain boundary on switching, we assumed a reduced transition temperature at the grain boundary of a bi-crystal (Fig. 1(c)). We studied two cases where the lowest transition temperatures at the grain boundary were assumed to be 150 °C and 25 °C, respectively. The transition temperature within the grain was 479 °C, the same as the transition temperature of bulk lead titanate under the clamped boundary condition. It was assumed that the transition temperature varied linearly near the grain boundary as
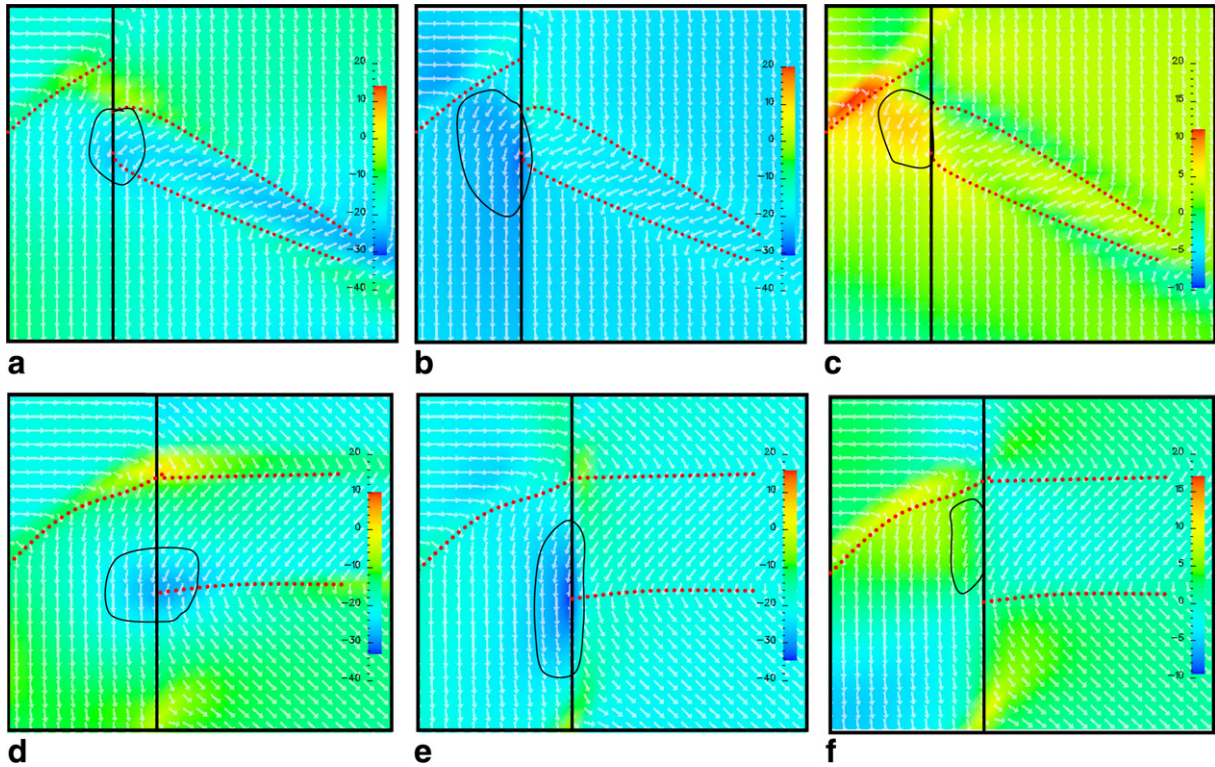
Fig. 8. Normalized global elastic stress distribution near the grain boundary of bi-crystal 1 and bi-crystal 2 during switching. The normalization factor (σ_0) is 9.8×10^6 MPa. (a)–(c) show the distributions of stress components σ_{11}^G/σ_0, σ_{22}^G/σ_0 and σ_{12}^G/σ_0 of bi-crystal 1 corresponding to the domain structure in Fig. 7(b) while (d)–(f) shows the distribution of similar stress components in bi-crystal 2 corresponding to the domain structure in Fig. 7(d). The grain boundary is shown by a thick line while the domain walls are schematically shown by a dotted line. The locations of stress concentration near the grain boundary are marked.

shown in Fig. 1(c). The grain boundary width was maintained at four simulation grid points, i.e. the width of the grain boundary was $4\Delta x_1^G$. The orientation of the bi-crystal was the same as described in Fig. 1(b). For the rest of the paper, bi-crystal 1 and bi-crystal 2 with a reduced transition temperature at the grain boundary will be referred as bi-crytsal 1′ and bi-crystal 2′, respectively.

Fig. 9(a) and (b) shows the hysteresis loops for bi-crystal 1′ and bi-crystal 2′. It can be seen that, in both the cases, the coercive field increased as the transition temperature at the grain boundary decreased. For bi-crystal 1', in which the transition temperature at the grain boundary was decreased from 479 °C to 25 °C, the increase in the coercive field was small. This can be explained from the switching behavior in bi-crystal 1 in Fig. 6(a), which was found to be similar to the single crystal with the coercive field approximately the average of the single crystal values. As the grain boundary did not play a significant role in the switching behavior of bi-crystal 1, reducing the transition temperature at the grain boundary only had a small effect on the coercive field. For the case of bi-crystal 2, the situation was quite different. As shown above, nucleation of the new domains in bi-crystal 2 occurred primarily at the grain boundary for bi-crystal 2 (Fig. 7(d)): a significantly lower transition temperature at the grain boundary greatly decreased the coupling across the grain boundary and thus,

increased the coercive field (Fig. 9(b)). Therefore, if this is the general case, a decrease in the ferroelectric transition temperature at the grain boundary will increase the coercive field.

4.3. Grain size effect on domain switching in a polycrystal

In order to study the effect of the grain size on the domain structure and polarization switching, we first employed a phase field model for grain growth for generating two-dimensional grain structures. Fig. 10 presents a polycrystal consisting of 54 grains. Each grain was assumed to be oriented along a different crystallographic direction. Orientations of different grains could be specified by the angle φ about the x_3^G axis. The grain orientations were limited to within 0° and 45° due to symmetry. In this work, the orientation of each individual grain (φ) was assigned randomly and did not change with time during domain switching. In order to study size effects on the domain structure and polarization switching we used six grain structures with different grain sizes and 512×512 discrete grid points, such that the average grain radius varies between 11 and 88 nm.

Fig. 11 shows the domain structures of the six polycrystals without any applied electric field. A comparison of the domain structures in Fig. 11(a)–(f) showed that, the larger
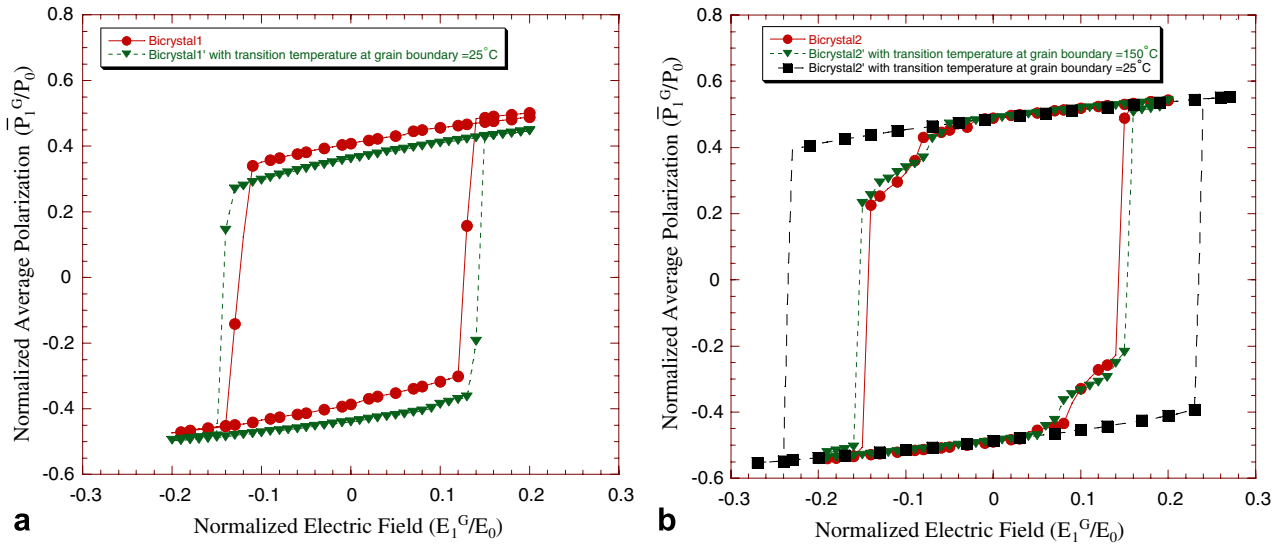
Fig. 9. Hysteresis loops of bi-crystals for two different orientations of grain 2 shown in Fig. 1(c): (a) for bi-crystal 1′; (b) for bi-crystal 2′. In each of the figures the lowest transition temperature at the grain boundary is varied.
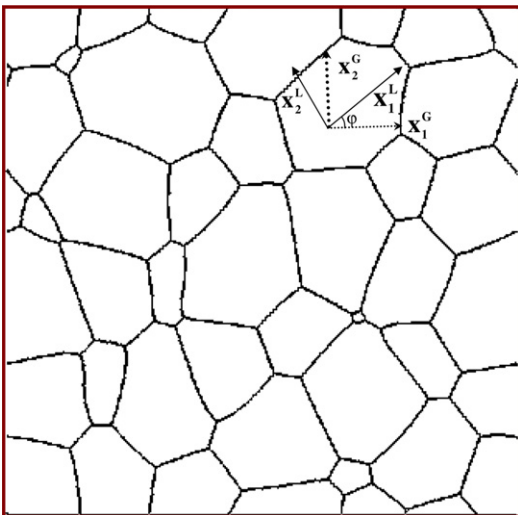

Fig. 10. Simulated grain structure using the grain growth model. The figure shows the two different coordinate systems used during calculations. G and L represent global and local coordinates, respectively. For each grain the direction of the global coordinate system remains fixed while the local coordinate system rotates such that $0° \leqslant \varphi \leqslant 45°$.

the average grain size, the higher the total number of tetragonal variants present in each grain. As the grain size decreased, the number of tetragonal variants present in each grain decreased. This prediction matched well with the experimentally observed domain structures in PZT [26]. Furthermore, we observed that, as the average grain radius decreased to 11 nm, most of the grains became single domains.

In order to study the effect of grain size on the switching behavior, we constructed the hysteresis loops for three grain sizes ($R_{ave} = 11$, 32 and 52 nm) as presented in Fig. 12. It is shown that the polycrystalline structure with a smaller grain size had a smaller magnitude of coercive field. It has been shown in Fig. 7(b) and (d) that grain boundaries act as sources for the nucleation of new domains during switching. As a result, a polycrystal with a smaller grain size provides more nucleation sites for new domains during switching and, thus, results in a lower coercive field. The remnant polarization for different grain sizes almost remains the same.

Although our prediction of the effect of grain size on the domain structure was consistent with experimental observation, the decrease in the coercive field with grain size from our simulations seemed to contradict other experimental observations [2–4] where it was observed that the coercive field increased with a decrease in the grain size. This difference in the grain size dependence on switching was possibly due to the much smaller grain size (of the order of few tens of nanometers) considered in our simulations as compared to those studied experimentally, which were in the order of microns. Hence, for a grain structure with an experimental grain size, each grain typically contains more than two different types of domain [27]. As our simulation results on the switching behavior of bi-crystals showed that the number of domains present within each grain affected the domain switching behavior of individual grains, it appears that the range of grain size considered in this work may not have been sufficient enough for explaining the experimental observation. Thus, it is difficult to draw clear conclusions on the effect of size on coercive fields based on our two-dimensional simulations.

Although the phase field model presented in this paper can be used for studying the switching behavior in three-dimensional ferroelectric polycrystals, we conducted our simulations in two dimensions for computational reasons. Owing to the two-dimensional nature of the simulations the focus of this paper was on the mechanisms, primarily in order to understand the domain switching mechanism, rather than on a quantitative comparison with
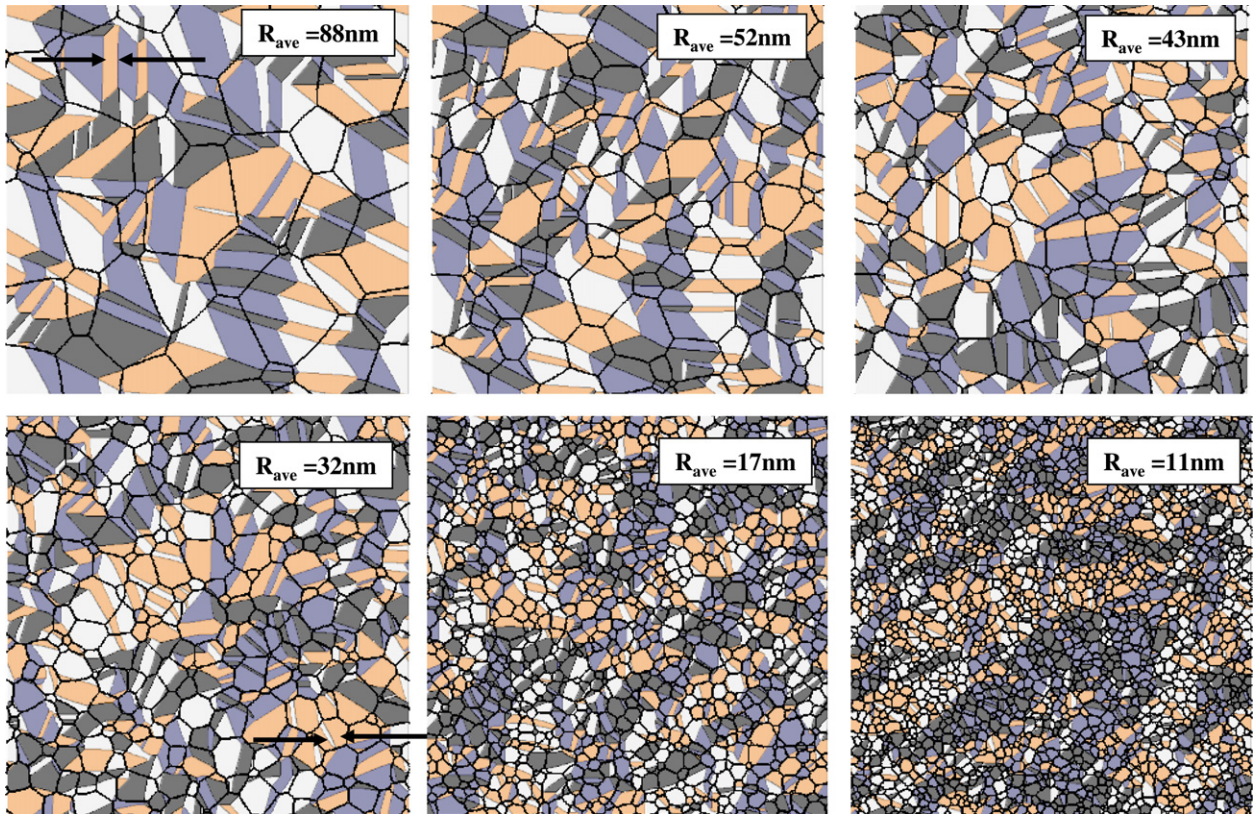
Fig. 11. Domain structure of lead titanate polycrystal in decreasing grain size. The system size is kept fixed in all the six cases at 512×512. The average grain radii are 88, 52, 43, 32, 17 and 11 nm, respectively.
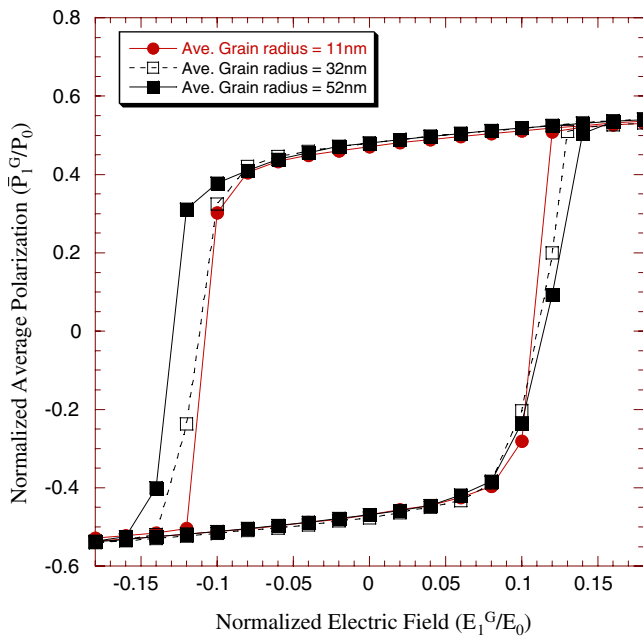

Fig. 12. Effect of grain size on the hysteresis loop obtained from phase-field simulations.

experimentally measured hysteresis loops. In fact, the study of the effect of the grain size on the coercive field in PZT using three-dimensional simulations is currently under way.

5. Conclusions

Phase field simulations were performed in order to understand the role of grain orientations and boundaries in domain switching in ferroelectric single, bi- and polycrystals. It was found that the switching behavior in a single crystal was strongly dependent on the orientation of the grain with respect to the applied electric field for both clamped and stress-free boundary conditions. It was observed that, in single crystals, the number of tetragonal variants in the domain structure at the maximum applied electric field determined the coercive field during polarization switching. The switching behavior of a bi-crystal was found to be similar to that in single crystals when the misorientation between the grains of a bi-crystal was less than 15°. The grain boundary was found to play a significant role in determining the switching behavior for bi-crystals with larger misorientations between the grains of the bi-crystal. Nucleation of new domains during polarization switching was found to occur at the grain boundary in bi-crystals, which led to high stress near the grain boundary. Furthermore, it was observed that reducing the transition temperature at the grain boundary might change the switching behavior of a bi-crystal. The effect of a reduction in the transition temperature at a grain boundary on the coercive field depended on the orientation of the grains with respect to the applied electric field

direction. Although the effect of grain size on the coercive field contradicted experimental observation, the result of the effect of grain size on domain structure was consistent with experiments.

Acknowledgements

References

[1] Auciello O, Scott JF, Ramesh R. Phys Today 1998;51:22.
[2] Randall CA, Kim N, Kucera JP, Cao WW, Shrout TR. J Am Ceram Soc 1998;81:677.
[3] Takeuchi T, Tabuchi M, Kondoh I, Tamari N, Kageyama H. J Am Ceram Soc 2000;83:541.
[4] Jin BM, Kim J, Kim SC. Appl Phys a-Mater Sci Proc 1997;65:53.
[5] Shaw TM, Trolier-McKinstry S, McIntyre PC. Ann Rev Mater Sci 2000;30:263.
[6] Tang XG, Wang J, Wang XX, Chan HL. Solid State Commun 2004;131:163.
[7] Hornebecq V, Huber C, Maglione M, Antonietti M, Elissalde C. Adv Funct Mater 2004;14:899.
[8] Hoffmann MJ, Hammer M, Endriss A, Lupascu DC. Acta Mater 2001;49:1301.
[9] Zhao Z, Buscaglia V, Viviani M, Buscaglia MT, Mitoseriu L, Testino A, et al. Phys Rev B 2004;70:024107.
[10] Zhang W, Bhattacharya K. Acta Mater 2005;53:199.
[11] Wada K, Kakimoto K, Ohsato H. J Appl Phys 2003;42:6149.
[12] Hu HL, Chen LQ. J Am Ceram Soc 1998;81:492.
[13] Ahluwalia R, Cao WW. Phys Rev B 2001;63:012103.
[14] Wang J, Shi SQ, Chen LQ, Li YL, Zhang TY. Acta Mater 2004;52:749.
[15] Li YL, Hu SY, Liu ZK, Chen LQ. Acta Mater 2002;50:395.
[16] Hwang SC, Arlt G. J Appl Phys 2000;87:869.
[17] Hwang SC, Huber JE, McMeeking RM, Fleck NA. J Appl Phys 1998;84:1530.
[18] Arlt G. Int Ferroelectrics 1997;16:229.
[19] Kim SJ. J Appl Phys 2002;92:2668.
[20] Rodel J, Kreher WS. J Eur Ceram Soc 2003;23:2297.
[21] Zhang W, Bhattacharya K. Acta Mater 2005;53:185.
[22] Li JY, Rogan RC, Ustundag E, Bhattacharya K. Nature Mater 2005;4:776.
[23] Choudhury S, Li YL, Krill III CE, Chen LQ. Acta Mater 2005;53:5313.
[24] Haun MJ, Zhuang ZQ, Furman E, Jang SJ, Cross LE. Ferroelectrics 1989;99:45.
[25] Chen LQ, Shen J. Comput Phys Commun 1998;108:147.
[26] Krill CE, Chen LQ. Acta Mater 2002;50:3057.
[27] Cao WW, Randall CA. J Phys Chem Solids 1996;57:1499.